



Confocal corrected attenuation coefficient imaging in phantoms and *in vivo* using chromatic focal shift calibration

JOHANNES KÜBLER,^{1,2}  VINCENT S. ZOUTENBIER,^{1,3} GIJS BUIST,^{1,3} JÖRG FISCHER,² ARJEN AMELINK,^{1,3} AND JOHANNES F. DE BOER^{1,4,*} 

¹LaserLaB, Department of Physics and Astronomy, Vrije Universiteit, Amsterdam, The Netherlands

²Heidelberg Engineering GmbH, Heidelberg, Germany

³Department of Optics, Netherlands Organization for Applied Scientific Research, TNO, Delft, The Netherlands

⁴Department of Ophthalmology, Amsterdam UMC, Amsterdam, The Netherlands

*j.f.de.boer@vu.nl

Abstract: Optical coherence tomography (OCT) is conventionally used for structural imaging of tissue. Calibrating the intensity values of OCT images can give information on the tissue's inherent optical properties, such as the attenuation coefficient, which can provide an additional parameter to quantify possible pathological changes. To obtain calibrated intensity values, the focus position and Rayleigh length of the incident beam need to be known. We explore the feasibility of extracting the focus position from an OCT scan acquired with a single focus setting using the chromatic aberration of the system. The chromatic focal shift of an OCT system is exploited to achieve different focus positions for sub-spectrum reconstructed OCT images. The ratios of these images are used to estimate the focus position. Reconstruction of a high-resolution B-scan from coherent addition of sub-spectrum confocal function corrected B-scans and subsequent high-resolution OCT attenuation coefficient imaging is demonstrated. Furthermore, we introduce a method to experimentally determine the chromatic focal shifts of an OCT system in phantoms and an *in vivo* human retina. These shifts are compared to the theoretically expected shifts calculated with ray tracing.

© 2023 Optica Publishing Group under the terms of the [Optica Open Access Publishing Agreement](#)

1. Introduction

Optical coherence tomography (OCT) is an imaging technology which is used for cross sectional and volumetric imaging of tissue structures. Conventionally, OCT is used to image the morphology of tissue and to detect pathologies due to structural changes, such as layer thinning. Calibrating the intensity values of the OCT image can give information on the tissue's inherent optical properties, such as the attenuation coefficient, which can provide an additional parameter to quantify possible pathological changes, and could indicate structural changes at sub-resolution length scales. Attenuation coefficients calculated from OCT images have been investigated as a potential biomarker for monitoring and diagnosis of glaucoma [1,2], oral cancer [3], renal tumors [4,5], rectal cancer [6], and for further applications such as atherosclerotic plaque characterization [7–9] and delineation of brain tumor margins [10]. Computation of the attenuation coefficients is commonly performed either by slope fitting, where a single scattering model describing attenuation through exponential decay is fitted to the OCT A-line over a depth where the sample is assumed to be homogeneous [11], or by using the depth resolved method introduced by Girard *et al.* [12] and Vermeer *et al.* [13]. Reliable and reproducible calculation of the attenuation coefficients from OCT data requires correcting for: a) sensitivity changes with depth (roll-off) [13,14], b) the depth dependent noise floor [13], and c) the confocal effect, which depends on

the focus position and the apparent Rayleigh length [15]. Roll-off and noise floor can easily be compensated for by using reference data [14]. To determine the confocal function, a calibration process is required. This is typically achieved by acquiring a focus series by either moving the sample through the focus or moving the objective [11,15,16], or by imaging a homogeneous low scattering sample. The confocal function depends on the actual sample and the optical system, e.g., in retinal imaging this includes the cornea and lens.

It has been shown that two scans of the same sample acquired with a different focus can be used to extract the confocal parameters [17–20]. A limitation of this method is that two scans of the same position are required, which doubles the acquisition time and can be cumbersome if the sample is moving or in the case of retinal imaging if the eye is also accommodating. Thus, there is a need for extracting the focus position from OCT scans without changing the focus.

In this work, we explore the feasibility of extracting the focus position from an OCT scan acquired with a single focus setting. We exploit the chromatic focal shifts of an OCT system allowing us to achieve different focus positions for sub-spectrum reconstructed OCT images and use the ratios of these images to estimate the focus positions. Reconstruction of a high-resolution B-scan from sub-spectrum confocal function corrected B-scans using coherent addition is demonstrated. We introduce a method to experimentally determine the chromatic focal shifts of an OCT system in phantoms and an *in vivo* human retina. These shifts are compared to the theoretically expected shifts calculated with ray tracing.

2. Methods

2.1. Theory

Here we give a short recapitulation on how the OCT signal including the confocal function can be modeled. Single backscattered light detected within an OCT A-line can be described by

$$I(z) \propto r(z)h(z)\alpha\mu_t(z)e^{-2\int_0^z \mu_t(u)du} \quad (1)$$

where z is the depth coordinate, with $z = 0$ defined as the sample surface, $r(z)$ is the sensitivity roll-off, $h(z)$ is the confocal function, α is the backscattered fraction of light, and $\mu_t(z)$ is the attenuation coefficient [13]. The depth dependent background has already been accounted for in Eq. (1) (see Section 2.6). For a single-mode fiber based system, the focused beam has a Gaussian intensity profile and the confocal function $h(z)$ can be described by

$$h(z) = \left[\left(\frac{z - z_f}{z_R} \right)^2 + 1 \right]^{-1} \quad (2)$$

with the focus position z_f and the Rayleigh length z_R .

The ratio of two aligned A-lines $I_1(z)$ and $I_2(z)$ of the same location acquired with a different focus position can be expressed by the ratio of the two confocal functions as

$$\frac{I_1(z)}{I_2(z)} = \frac{\left(\frac{z - (z_{f1} + \Delta z_f)}{z_R} \right)^2 + 1}{\left(\frac{z - z_{f1}}{z_R} \right)^2 + 1} \quad (3)$$

where $\Delta z_f = z_{f2} - z_{f1}$ is the axial focus shift, with the focus positions z_{f1} and z_{f2} of the numerator and denominator A-line, respectively. Eq. (3) can be utilized to extract the confocal function parameters from OCT data acquired at the same location but with different focus positions [17–20].

In spectral domain OCT (SD-OCT) a short-time Fourier transform (STFT) can be performed in order to obtain sub-spectral A-lines for different frequency windows w_i [21,22]. The windowing

function $w_i(k - k_i)$ is applied to the spectral data prior to the Fourier transform, where k denotes the wavenumber and k_i the center of the windowing function that is shifted along the whole spectrum. If the OCT system has a chromatic focal shift, different sub-spectral A-lines of the same A-scan have different confocal functions (Fig. 6(a)) and the ratio of two A-lines of a homogeneous sample calculated with different spectral windows w_i and w_j with the mean wavelengths λ_i and λ_j can be expressed as

$$\frac{I(z, \lambda_i)}{I(z, \lambda_j)} = \frac{\overbrace{\left(\frac{z - (z_f(\lambda_i) + \Delta z_{f,i})}{z_R(\lambda_j)} \right)^2 + 1}^C}{\overbrace{\left(\frac{z - z_f(\lambda_j)}{z_R(\lambda_j)} \right)^2 + 1}^B} \frac{\overbrace{\alpha(\lambda_i)\mu_t(\lambda_i)}^A}{\alpha(\lambda_j)\mu_t(\lambda_j)} e^{2z\Delta\mu_{j,i}} \quad (4)$$

with $\Delta z_{f,i} = z_f(\lambda_j) - z_f(\lambda_i)$ and $\Delta\mu_{j,i} = \mu(\lambda_j) - \mu(\lambda_i)$. We explored the feasibility of using Eq. (4) to extract the focus position from the ratio of sub-spectral A-lines acquired with a single focus setting with a setup that has a chromatic focal shift.

2.2. OCT system

OCT measurements were performed with a high-resolution SD-OCT device based on the SPECTRALIS platform (Heidelberg Engineering GmbH, Heidelberg, Germany). The system uses a light source with a central wavelength of 853 nm and a bandwidth of 137 nm, and it has an A-scan rate of 85 kHz. Many B-scans of the same location can be averaged together using the active tracking capability of the device. By using the SPECTRALIS' refraction error compensation mechanism, the focus position can be changed. The focus setting in diopters (1/m) was saved with each data set.

2.3. Model eye with intralipid and layered titanium oxide sample

As previously described [20], for phantom measurements, a model eye was used featuring an 18 mm focal length planoconvex lens (01LPX015, Melles Griot, anti-reflection coating on the convex side) and a water filled chamber that can hold different types of samples.

To obtain a homogeneous scattering phantom, a dilution of 1.24% volume intralipid was produced by diluting an intralipid 20% emulsion (I141-100ML, Sigma-Aldrich, Saint Louis, MO, USA) with distilled water. A cuvette (Macro cell 100-5-20, Hellma GmbH & Co. KG, Müllheim, Germany) was filled with the dilution and imaged inside the model eye with a scan angle of 9 degrees. The nominal scattering coefficients of the dilution for the OCT wavelengths (Fig. 8, blue line) were calculated by linear interpolation of the scattering coefficient for intralipid 20% described by Michels *et al.* [23]. The refractive index of the dilution was assumed to be equal to the refractive index of water and the absorption coefficient of the intralipid sample was assumed to be negligible ($\mu_s \gg \mu_a$, and $\mu_t = \mu_s$) [23].

A layered silicone-based phantom was fabricated as described by [20] and similar to the method outlined by de Bruin *et al.* [24], where the scattering coefficient is controlled by varying the percent weight of TiO_2 in the final elastomer (Table 1). The layered phantom was created by casting three thin films of the substrate with different scatterer concentrations on top of each other and afterwards stacking five of these layers. The emphasis for this sample was on ensuring the reproducibility of consistent scattering properties for layers at varying depths within the sample, rather than achieving specific attenuation coefficients for the layers [20]. This phantom was imaged inside the model eye. To allow averaging in both lateral dimensions, a small volume with a scan angle of 9 by 0.5 degrees was acquired consisting of 120 B-scans. The refractive index of the phantoms was assumed to be 1.42 [24], and the absorption coefficient was neglected ($\mu_t = \mu_s$), as no absorbers were added.

Table 1. Percent weight of TiO₂ and mean calculated attenuation coefficients with the corresponding standard deviations of the silicone-based layered phantom depicted in Fig. 11 (a).

Layer	TiO ₂ % weight	μ_t (mm ⁻¹)
A1	0.136	2.15 ± 1.28
B1	0.023	0.32 ± 0.53
C1	0.273	6.22 ± 2.41
A2	0.136	2.32 ± 1.34
B2	0.023	0.31 ± 0.41
C2	0.273	6.13 ± 1.95

2.4. Human retina

To demonstrate the applicability of our analysis to *in vivo* data, retinal scans of 12 by 1 degrees consisting of 120 B-scans were obtained in one subject using the tracking capability of the device to ensure acquisition at the same location for different focus settings. To avoid accommodation during the measurement an external fixation target was used for the fellow eye. This paper represents a feasibility study with the focus on the evaluation and correction algorithms and not a systematic analysis of clinical data. A written declaration of informed consent was obtained from the subject.

2.5. Ray tracing

To determine the expected chromatic focal shift (longitudinal chromatic aberrations) of the whole optical setup sequential ray tracing was performed using Zemax OpticStudio 22.1 (Zemax LLC, Kirkland, WA, USA). The human eye was simulated using the Navarro eye model [25]. The results of these simulations were compared to the experimentally extracted chromatic focal shift described in Section 2.7 and later used as input ($\Delta z_{f,i}$) for Eq. (4) as described in Section 2.8.

2.6. B-scan processing

All the data processing was performed using custom-written software in Python 3.7 (Python Software Foundation) and MATLAB 2021b (The MathWorks, Inc.). After dividing the raw spectra by a reference spectrum to reduce fixed pattern noise and linearizing the signal in wavenumber, a STFT was performed using the seven Hann windows shown in Fig. 1. The windows were chosen to balance spectral and spatial resolution, and processing time. In addition, the sum of the sub-spectral windows was applied prior to the Fourier transform to obtain a B-scan for the whole spectrum.

Before applying the two fitting procedures described in the following Sections 2.7 and 2.8 the resulting complex B-scans were processed further. First, to obtain intensity values the complex B-scans were squared. Second, the depth dependent background was subtracted, which was measured by acquiring B-scans without a sample. Third, to account for sensitivity changes with depth, roll-off was corrected for, which was measured by moving a mirror through the sampling depth of the OCT scan [14]. Fourth, to reduce speckle noise and average over imaging artifacts, 120 B-scans were averaged for each spectral window. Because the B-scans were part of a small volume, this resulted in lateral averaging along the slow scan axis, with filter kernel sizes of 157 μm for the phantoms and 293 μm for the retina. Finally, to suppress high frequency noise a two-dimensional Gaussian filter with a standard deviation of 5 pixels (laterally 18.45 μm for the two phantoms and 23.25 μm for the retina, axially 9.65 μm for intralipid, 9 μm for the layered phantom, and 9.4 μm for the retina) and a moving mean filter in the fast scan direction with

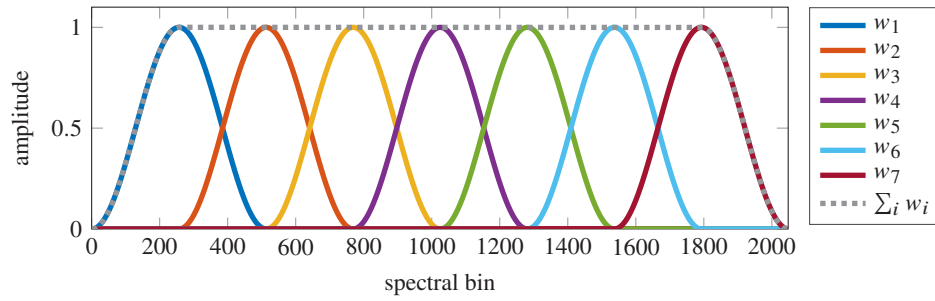


Fig. 1. Spectral windows used to obtain sub-spectral B-scans (solid) and the full spectral window (dashed). The spectral bins are linearly distributed across a k range from 8039 m^{-1} to 6802 m^{-1} . The mean wavelengths of the sub-spectral windows from left to right are 797 nm, 813 nm, 830 nm, 847 nm, 865 nm, 884 nm, and 903 nm.

a window size of 11 pixels ($40.59 \mu\text{m}$ for the two phantoms and $51.15 \mu\text{m}$ for the retina) was applied to each mean B-scan.

2.7. Spectrally resolved focus ratio fit

In this section we describe a method that allows for the independent determination of the focus position for different wavelengths across the OCT spectrum. Consequently, the chromatic focal shift present in the imaging system was extracted from the OCT data itself. Throughout this work, we refer to this method as the spectrally resolved focus ratio fit or just focus ratio fit.

In order to extract the confocal functions for different wavelengths we took the ratios of filtered sub-spectrum mean B-scans calculated with the same spectral window but acquired with different focus positions. We fitted Eq. (3) with the focus position z_f and the apparent Rayleigh length z_R as free parameters using a Levenberg-Marquardt nonlinear least squares algorithm (MATLAB function `fitlm`) to every A-line ratio. The focus ratio fit was performed for all possible combinations of the different focus settings and a mean confocal function for each focus setting and spectral window was calculated following the procedure described in [20]. To obtain the confocal function for the full OCT spectrum the focus ratio fit was also applied to the mean B-scans of the whole spectrum.

2.8. Spectral ratio fit

With the method described here we evaluated the feasibility of extracting the focus position from OCT data acquired with a single focus setting. The same principle of using A-lines with different confocal functions described in Section 2.7 was exploited. However, instead of using A-lines of the same position acquired with different focus settings, A-lines of the same position and acquisition calculated with different sub-spectral windows were used. The ratios of different sub-spectral mean A-lines were calculated after normalization with their integral over the whole depth range. If the OCT system has a considerable chromatic focal shift the ratio of the confocal functions (denoted with C in Eq. (4)) dominates Eq. (4). To extract the focus position we fitted this equation to the A-line ratios with the two free parameter z_f and $\Delta\mu_{j,i}$. The part denoted with B in Eq. (4) was assumed to be close to one due to the normalization. To reduce fitting parameters, the Rayleigh lengths $z_R(\lambda)$ measured with the spectrally resolved focus ratio fit (Section 2.7) and the chromatic focal shifts obtained from ray tracing (Section 2.5) $\Delta z_{f,i}$ were used in the equation. Even though Eq. (4) is only fully valid for homogeneous samples, we also applied it to heterogeneous samples assuming a marginal wavelength dependence of the attenuation difference within the spectral range of the OCT system that can be approximated with the single $\Delta\mu_{j,i}$ fit parameter. In this work, we refer to this method as the spectral ratio fit.

2.9. Calculate full resolution confocal function corrected B-scan

The confocal functions, determined for the sub-spectral B-scans using the spectral ratio fit, can be used to correct the A-lines of the sub-spectra individually. This results in different confocal function corrected B-scans for the different wavelengths with a lower resolution than the B-scan of the full spectrum. To obtain a high-resolution, confocal function corrected B-scan, we processed the complex sub-spectral B-scans as follows:

1. The individual sub-spectral complex A-lines consisting of amplitude and phase were roll-off corrected and divided by the square root of the confocal function obtained for the respective spectral window.
2. The corrected sub-spectral complex A-lines were transformed back to k-space and the resulting spectra were added coherently. This produced spectra covering the full spectral range.
3. The full spectra were transformed to z-space and the complex A-lines squared to obtain intensity values.
4. Steps 1 to 3 were also carried out for an OCT scan that was acquired without a sample. This depth dependent background was subtracted.
5. To average over imaging artifacts and to reduce speckle noise 120 B-scans were averaged resulting in a high-resolution mean B-scan that was individually corrected for the sub-spectral confocal functions.

For *in vivo* measurements the individual 120 B-scans are not necessarily in perfect alignment due to eye movements. Because the confocal functions and thus the focus positions were calculated from a mean B-scan, where the individual B-scans were matched on top of each other using affine transformations, the inverse affine transformations were used to transform the focal plane extracted from the mean B-scan back to the individual B-scans.

To visualize the difference between adding the intensities of the A-lines calculated from sub-spectral bands, and coherent addition of the sub-spectra and subsequent calculation of an A-line for the full spectrum, the corresponding intensity A-lines are shown in Fig. 2. The A-lines were obtained from an OCT scan of the human retina without any correction of noise floor or roll-off. At first glance, one would expect that the squared amplitude of the coherently added sub-spectra (dashed gray) has a significantly higher signal to noise ratio (SNR) than the sum of the squared amplitudes of the individual sub-spectral A-lines (thick dark green). The SNR in SD-OCT is given by $\text{SNR} = P_s \tau_i / E_v$, the reflected sample arm power P_s times the integration time τ_i divided by the photon energy E_v [26]. However, this SNR is defined as an SNR for the full A-line. The SNR per depth resolution (defined by the spectral width of the source) is given by the SNR expression multiplied by the depth resolution over the A-line length. The intensity A-line for the coherently added sub-spectra has a much higher resolution than an A-line for the sum of the squared amplitudes of the sub-spectra. The SNR per depth resolution is therefore virtually equal for the sum of the squared amplitudes of the sub-spectra and for the high-resolution A-line of the coherent sum of sub-spectra, which is observed in Fig. 2.

2.10. Attenuation coefficient calculation

After confocal function correction the attenuation coefficients were calculated using the depth resolved method described by Vermeer *et al.* [13]. It is based on two main assumptions: (1) all the light is attenuated within the range of the A-scan; and (2) the backscattered light detected by the OCT system is a fixed fraction of the attenuation coefficient, i.e., the backscattering fraction is constant throughout the sample depth.

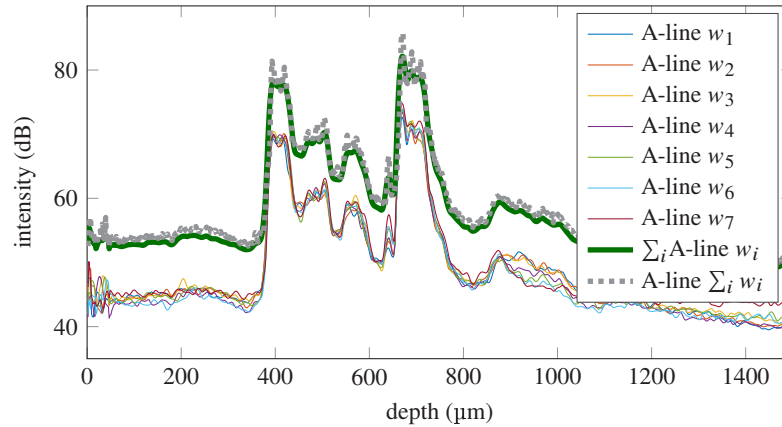


Fig. 2. A-lines for the 7 different spectral windows (thin solid), sum of the A-lines calculated with the sub-spectra (thick dark green), and A-line calculated using coherent addition of the full spectrum (dashed gray).

3. Results

3.1. Simulated chromatic focal shift versus measured shift

Figure 3 shows the comparison between the chromatic focal shift simulated with ray tracing (blue), as described in Section 2.5, and the shift extracted experimentally with the spectrally resolved focus ratio fit method (orange), as described in Section 2.7. The experimental values were determined by calculating the mean and standard deviation of the chromatic focal shifts of all A-lines of the B-scans acquired with different focus settings. The ray tracing agrees well with the focus ratio fit results for the two model eye samples (intralipid, layered TiO_2). The simulation result for the Navarro eye model is slightly lower than the experimentally extracted chromatic focal shift of the *in vivo* data, but still well within the standard deviation. The close agreement supports the approach of taking the simulated chromatic focal shift $\Delta z_{f,i}$ as an input to Eq. (4) when performing the spectral ratio fit.

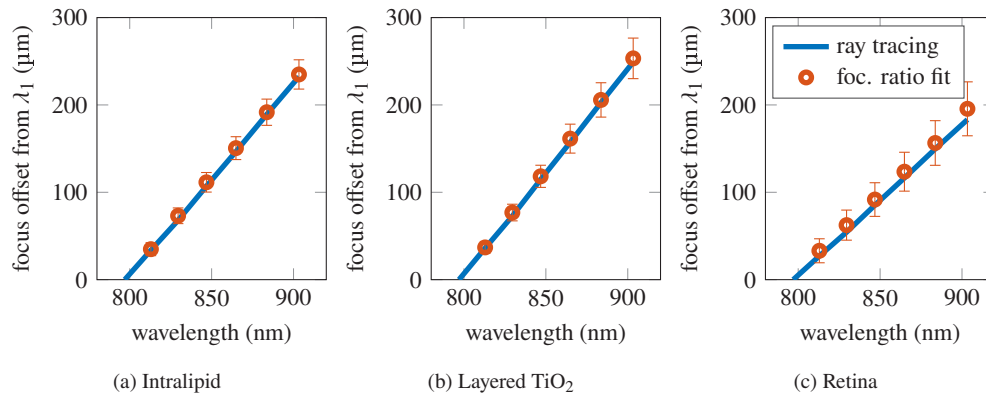


Fig. 3. Chromatic focal shift as calculated with ray tracing (blue line) and the focus ratio fit method (orange circles). The error bars represent standard deviations.

3.2. Homogeneous intralipid phantom

Figure 4 shows the mean Rayleigh lengths extracted with the focus ratio fit method for the different sub-spectra and for the full spectrum. With longer wavelengths the Rayleigh lengths show a slight increase. For the full spectrum the Rayleigh length is slightly larger than for any of the sub-spectra. The extracted focal planes for three different focus settings using both the focus ratio fit and the spectral ratio fit method are shown in Fig. 5. For better visualization, the focus ratio fit focal planes were smoothed by fitting a second order polynomial. It can be observed that the focus ratio fit is able to extract focal planes for the different sub-spectral B-scans (dashed lines), with mean wavelengths of 797 nm (blue), 813 nm (orange), 830 nm (yellow), 847 nm (purple), 865 nm (green), 884 nm (light blue), and 903 nm (dark red). For foci close to the sample surface (Fig. 5(a)) the focal planes extracted with the spectral ratio fit deviate from the focal planes extracted with the focus ratio fit, which are further up in the B-scan. For foci approximately 200 μm to 520 μm within the sample (Fig. 5(b)) the focal planes for both methods agree well. Further within the sample (Fig. 5(c)) the focal planes extracted with the focus ratio fit are below the spectral ratio fit extracted focal planes.

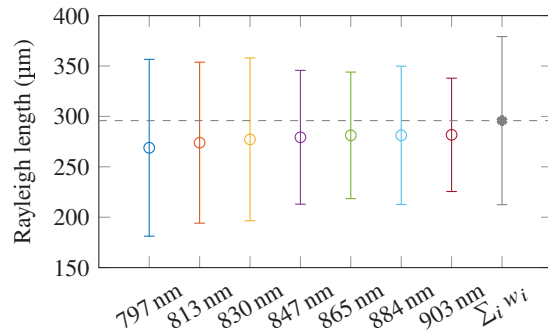


Fig. 4. Mean Rayleigh lengths and corresponding standard deviations obtained in the intralipid sample from the focus ratio fit for the sub-spectral bands and for the full spectrum. The mean wavelengths of the sub-spectra are indicated on the x-axis and the dashed line represents the Rayleigh length extracted for the full spectrum.

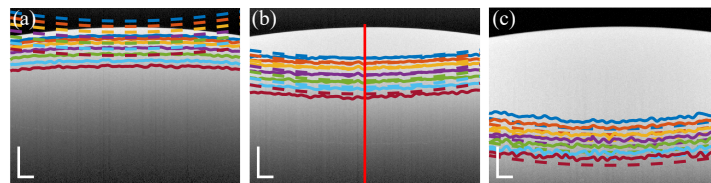


Fig. 5. B-scans of the intralipid sample acquired with different focus positions. Dashed lines are the focal planes for the different mean wavelengths extracted with the focus ratio fit and the solid lines the focal planes extracted with the spectral ratio fit. The colors correspond to the different sub-spectral windows specified in Fig. 1. The red vertical line in (b) indicates the location of the mean A-lines plotted in Fig. 6. The scale bars are 200 μm in each dimension.

To visually demonstrate the effect of the chromatic focal shift, the mean sub-spectrum A-lines obtained from the homogeneous intralipid sample can be seen in Fig. 6(a). They were calculated by averaging the 61 central A-lines of an averaged B-scan (location indicated in Fig. 5(b)). The effect of the confocal function and the chromatic focal shift can clearly be observed. The confocal function corrected A-lines using the focus position obtained with the spectral ratio fit method are

shown in Fig. 6(b). The different slopes in Fig. 6(b) represent the different scattering coefficients as a function of wavelength, as is also demonstrated in Fig. 8. The effectiveness of individually correcting for the confocal function of different sub-spectral A-lines and coherent summation to obtain an A-line for the full spectrum using the method described in Section 2.9 is illustrated in Fig. 7. It shows a mean A-line calculated for the full spectral window before correcting for the confocal function, and after correction. The uncorrected mean A-line exhibits the effect of the confocal function on the signal decay. This nonlinear part of the decay is removed in the corrected mean A-line.

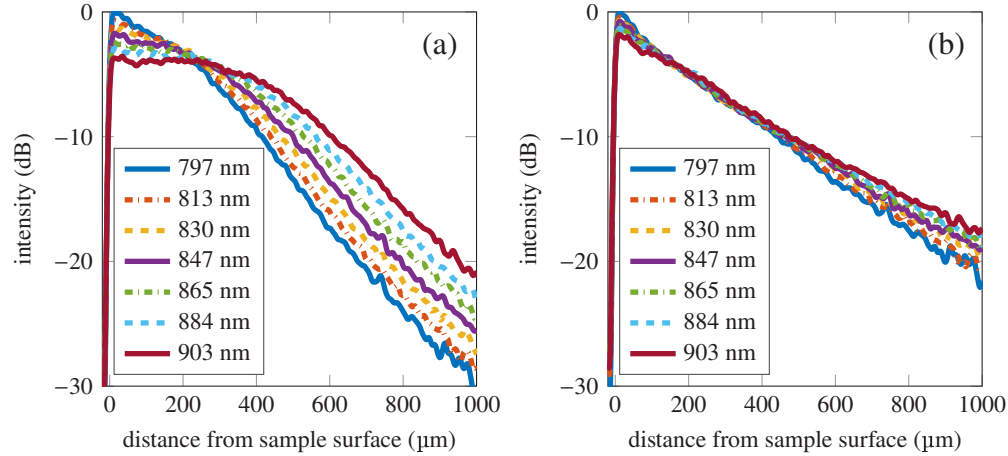


Fig. 6. (a) Sub-spectral mean A-lines of a homogeneous intralipid sample (nominal μ_s of 2 mm^{-1} at the central wavelength), the mean wavelengths of the spectral windows are given in the legend. (b) Confocal function corrected A-lines, where the focus position has been extracted using the spectral ratio fit method.

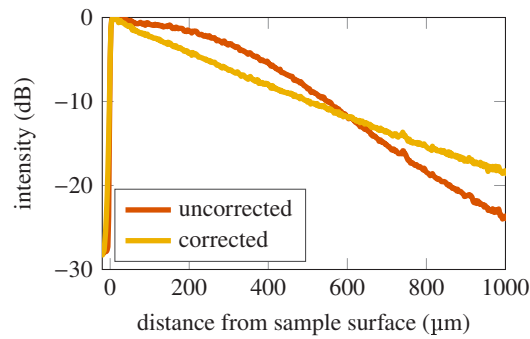


Fig. 7. Mean A-line of the intralipid phantom calculated using the full spectral window before confocal function correction (orange), and A-line after correcting for the confocal functions of different spectral windows and transformation back to a full window A-line (yellow), as described in Section 2.9.

The mean attenuation coefficients obtained with the depth resolved method [13] for the different wavelengths are plotted in Fig. 8, which are close to the expected values after correcting for the confocal function.

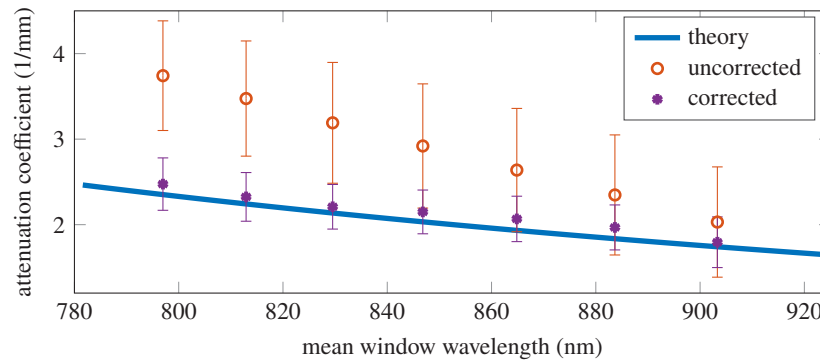


Fig. 8. Calculated wavelength dependent attenuation coefficients of the homogeneous intralipid sample for the uncorrected A-lines (red), and the spectral ratio fit confocal function corrected A-lines (purple). Error bars represent standard deviations. The blue line indicates the expected attenuation coefficient based on [23].

3.3. Layered TiO_2 phantom

Figure 9 shows the mean Rayleigh lengths extracted with the focus ratio fit method for the different sub-spectra and for the full spectrum for the layered TiO_2 phantom. With longer wavelengths the Rayleigh lengths show a slight increase. For the full spectrum the Rayleigh length is larger than for any of the sub-spectra. The focal planes obtained for different focus settings for the central spectral window w_4 with both methods, the focus ratio fit, and the spectral ratio fit, are compared in Fig. 10 (a). For better visualization, the focus ratio fit focal planes were smoothed by fitting a second order polynomial. For foci within the first 200 μm of the sample the spectral ratio fit extracted focal planes (solid lines) are below the focal planes obtained with the focus ratio fit (dashed lines). For deeper focus positions focal planes extracted with the two methods are in good agreement but a slight deviation can be observed with further increasing focus position. The focal planes of all seven sub-spectral B-scans are shown in Fig. 10 (b) for the focus indicated with a white arrow in Fig. 10 (a). Here, both methods agree well in the lateral parts of the B-scan and in the center focal planes extracted with the spectral ratio fit are slightly higher up compared to the ones extracted with the focus ratio fit. The attenuation coefficient map for the full spectrum, after correction of the sub-spectral confocal function as described in Section 2.9, is shown in Fig. 11 (a), and the corresponding mean values for the different layers are illustrated in Fig. 11 (b) and listed in Table 1. Layers with the same TiO_2 concentration exhibit similar attenuation coefficients independent of their depth within the sample. The relatively large standard deviations reflect the fact that the different layers are not perfectly homogeneous, as can be seen in Fig. 11 (a).

3.4. Human retina

Figure 12 shows the mean Rayleigh lengths extracted with the focus ratio fit method for the different sub-spectra and for the full spectrum for the *in vivo* retinal data. In contrast to the phantoms, here, the measured Rayleigh lengths become shorter with increasing wavelength and the Rayleigh length of the full spectrum is similar to the ones for the first two spectral windows. The focal planes obtained in the human retina for various focus settings, with the focus ratio fit (dashed lines) and the spectral ratio fit (solid lines), are shown in Fig. 13 (a) for the central spectral window w_4 . For better visualization, the focus ratio fit focal planes were smoothed by fitting a second order polynomial. For foci above and within the retinal nerve fiber layer (RNFL) the focus extracted with the spectral ratio fit is deeper than the focus extracted with the focus ratio

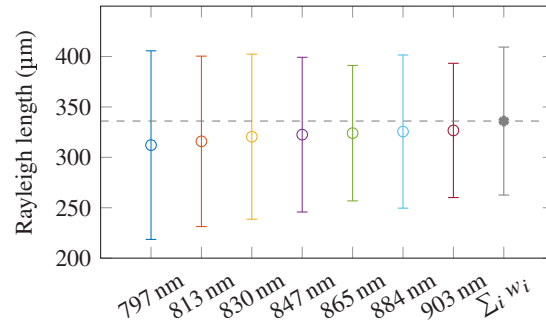


Fig. 9. Mean Rayleigh lengths and corresponding standard deviations obtained in the layered TiO_2 sample from the focus ratio fit for the sub-spectral bands and for the full spectrum. The mean wavelengths of the sub-spectra are indicated on the x-axis and the dashed line represents the Rayleigh length extracted for the full spectrum.

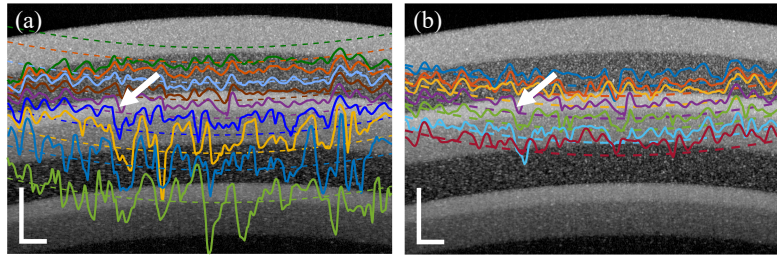


Fig. 10. OCT B-scans of the layered TiO_2 phantom. Dashed lines are the focal planes extracted with the ratio fit method using B-scans acquired with different focus settings and smoothed by fitting a second order polynomial. Solid lines are extracted by using the spectral ratio fit method. (a) Focal planes for spectral window number 4 for nine different focus settings. (b) All 7 spectral focal planes for the single focus setting indicated with a white arrow in (a) and (b). The colors in (b) correspond to the different sub-spectral windows specified in Fig. 1. The scale bars are $200\ \mu\text{m}$ in each dimension.

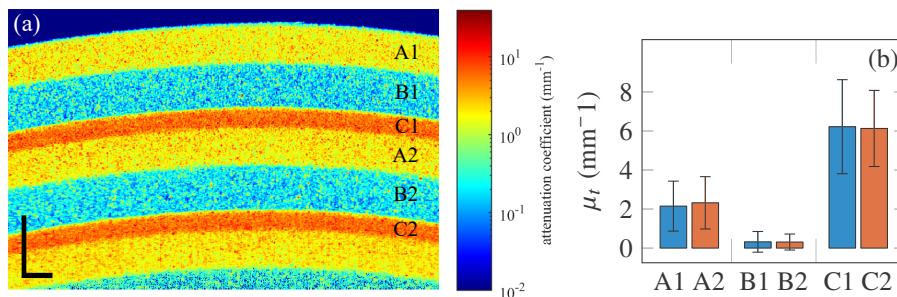


Fig. 11. (a) Attenuation coefficient map of the layered TiO_2 phantom for the full spectrum corrected for the sub-spectral confocal functions. The scale bars are $200\ \mu\text{m}$ in each dimension. The corresponding mean attenuation coefficients and standard deviations are shown in (b) and listed in Table 1.

fit. Within the ganglion cell layer (GCL) and down to the retinal pigment epithelium (RPE) the foci of spectral and focus ratio fit largely overlap. Below the RPE the results of the two methods start to deviate again with the spectral ratio fit focal plane being higher up in the sample than the focus ratio fit plane. The focal planes of all seven sub-spectral B-scans are shown in Fig. 13 (b) for the focus indicated with a white arrow in Fig. 13 (a). Figure 14 (a) shows the confocal function corrected attenuation coefficient map for the central sub-spectral window w_4 . The high-resolution attenuation coefficient map corresponding to the full spectrum, after correction of the sub-spectral confocal functions extracted with the spectral ratio fit as described in Section 2.9, is shown in Fig. 14 (b). The corresponding mean values for the different retinal layer segments shown in Fig. 14 (c) are listed in Table 2. To calculate the mean attenuation coefficient for each layer segment, locations with large blood vessels were excluded (Fig. 14 (b), marked in red) because here the extracted focal planes exhibit a deviation and the strong absorption of blood clearly violates the assumption of a constant backscattering fraction for the depth resolved method. Note that the large standard deviations in Table 2 originate from the structures apparent within the segmented layers (Fig. 14 (c)).

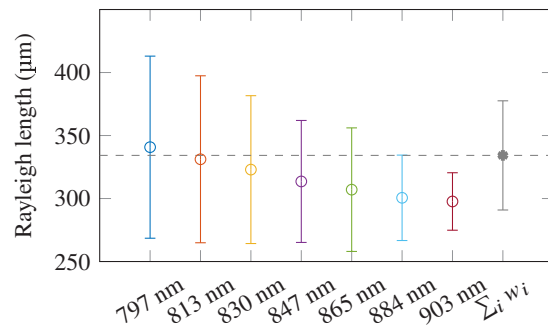


Fig. 12. Mean Rayleigh lengths and corresponding standard deviations obtained in the *in vivo* retina from the focus ratio fit for the sub-spectral bands and for the full spectrum. The mean wavelengths of the sub-spectra are indicated on the x-axis and the dashed line represents the Rayleigh length extracted for the full spectrum.

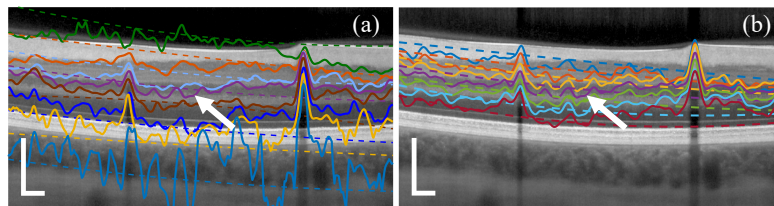


Fig. 13. OCT B-scans of a human retina. Dashed lines are the focal planes extracted with the ratio fit method using B-scans acquired with different focus settings and smoothed by fitting a second order polynomial. Solid lines are extracted by using the spectral ratio fit method. (a) Focal planes for spectral window number 4 for eight different focus settings. (b) All 7 spectral focal planes for the single focus setting indicated with a white arrow in (a) and (b). The colors in (b) correspond to the different sub-spectral windows specified in Fig. 1. The scale bars are 200 μm in each dimension.

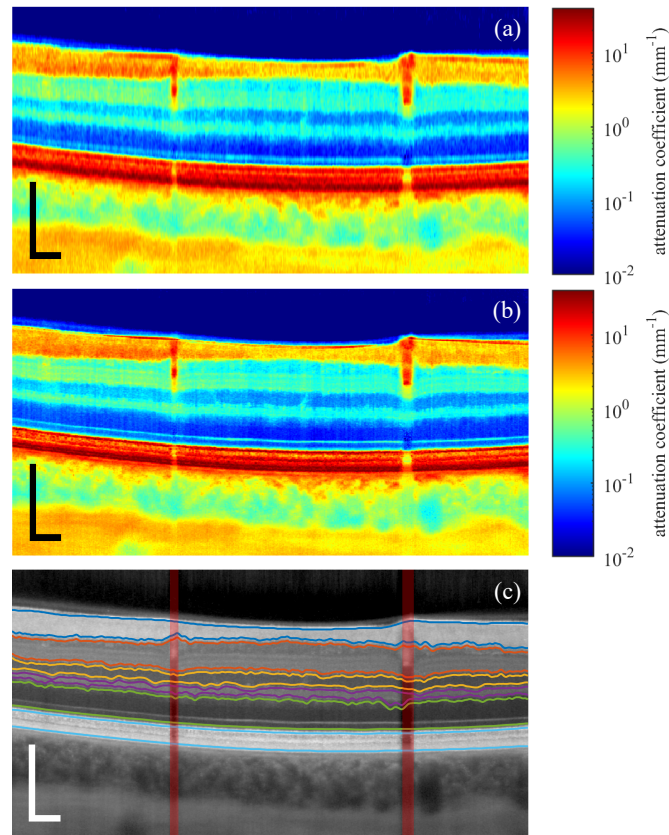


Fig. 14. (a) Attenuation coefficient map of a human retina for the central sub-spectral window w_4 . (b) High-resolution attenuation coefficient map for the full spectrum corrected for the sub-spectral confocal functions. (c) Segmented retinal layers from top to bottom are retinal nerve fiber layer (RNFL), ganglion cell and inner plexiform layer (GCL&IPL), inner nuclear layer (INL), outer plexiform layer (OPL), outer nuclear layer (ONL), and photo receptor and retinal pigment epithelium (PR&RPE). The corresponding mean attenuation coefficients for the full spectrum of the layers indicated in (c) are listed in Table 2. The locations with large blood vessels indicated in (c) were excluded. The scale bars are $200\ \mu\text{m}$ in each dimension.

Table 2. Mean attenuation coefficients and corresponding standard deviations for the full spectrum corrected for the sub-spectral confocal functions of the retinal layers indicated in Fig. 14 (c).

Retinal layer	$\mu_t\ (\text{mm}^{-1})$
retinal nerve fiber layer (RNFL)	3.50 ± 1.44
ganglion cell and inner plexiform layer (GCL&IPL)	0.41 ± 0.20
inner nuclear layer (INL)	0.12 ± 0.04
outer plexiform layer (OPL)	0.31 ± 0.10
outer nuclear layer (ONL)	0.07 ± 0.05
photo receptor and retinal pigment epithelium (PR&RPE)	16.53 ± 9.81

4. Discussion

We demonstrate a technique to extract the confocal function for attenuation coefficient imaging by using the chromatic focal shift within a B-scan to find the focal plane. The present chromatic focal shift of an OCT system is exploited by utilizing the fact that for one single broad band OCT A-scan the spectrum can be split into sub-bands which enables calculation of A-lines for different wavelengths and subsequently with different focus positions. In return, this facilitates application of the previously published ratio fit method [16–18,20] to extract the focus position. Instead of applying the fitting method to the ratio of A-lines acquired with different focus settings, it is applied to the ratio of sub-spectral A-lines of the same acquisition to find the focus position. However, if the attenuation coefficients are wavelength dependent, taking the ratio of sub-spectral A-lines does not completely cancel out the structure in the A-line ratio (as represented by term A and B in Eq. (4)). Nevertheless, we demonstrate that assuming B of Eq. (4) to be close to one and only using A to account for wavelength dependent differences in the attenuation, within a certain focus position range, the spectral ratio fit can extract the focal planes. We show the method for a homogeneous intralipid sample, a layered TiO_2 phantom, and for *in vivo* retinal OCT data. The most robust results are obtained if the focus is located more than $200\text{ }\mu\text{m}$ and less than $600\text{ }\mu\text{m}$ within the sample, and for retinal imaging, if the focus is between the GCL and the RPE. For the intralipid sample, where the wavelength dependence has been published [23], we show that correcting the sub-spectral A-lines for the individual confocal function allows calculation of the attenuation coefficient for different mean wavelengths. This also shows that assuming $B = 1$ (Eq. (4)) is an approximation, aiming to limit the number of fitting parameters. A further refinement of the model could include an iterative loop to determine the actual value of B , based on a measurement as illustrated in Fig. 8. In the presented spectral ratio fit method, the Rayleigh length is not subject to fitting, as it is treated as a system parameter requiring calibration only once. For *in vivo* retinal measurements, an additional correction factor could be incorporated to accommodate variations in eye lengths. The bandwidth of the light source used in our experiments is fairly large (137 nm), resulting in a chromatic focal shift across the spectrum of more than $200\text{ }\mu\text{m}$ (Fig. 3). Recent work [20] has shown that a focal shift of about $100\text{ }\mu\text{m}$ is required for a robust ratio fit. If an OCT system with a smaller bandwidth or different central wavelength is used, the design of the optical elements could be adjusted to ensure sufficient longitudinal chromatic focal shift. Using a smaller bandwidth with adequate focal shift could actually minimize the effect of wavelength dependent attenuation.

We also introduce a procedure to extract the chromatic focal shift of an OCT system from OCT data. By performing a STFT on OCT data acquired with different focus positions, sub-spectral B-scans are obtained that can be used to extract the focus positions using the ratio fit method. The experimental results from a model eye and *in vivo* agree well with the chromatic focal shifts obtained with ray tracing for the model eye and the Navarro eye model [25], respectively. The proposed method can be used to characterize the chromatic focal shift of an OCT system if the exact optical components are unknown (e.g., in retinal imaging) or to validate optical simulations experimentally. Additionally, using the focus ratio fit, the wavelength dependent Rayleigh lengths are extracted for the three samples. These values are used as an input for the spectral ratio fit. The relatively large error bars for the extracted Rayleigh lengths indicate that the focus ratio fit method is not very sensitive to changes in this parameter. For the two phantom samples a slight increase of the sub-spectral Rayleigh lengths with wavelength is observed, as expected theoretically. The Rayleigh length of the full spectrum is larger than for the sub-spectra, which can originate from a convolution of the chromatically shifted confocal functions associated with the sub-spectra. For the *in vivo* data, the sub-spectral Rayleigh lengths decrease with longer wavelengths, possibly due to more multiple scattering for shorter wavelengths. The increase of measured apparent Rayleigh length with increasing scatterer concentration and consequently increasing multiple scattering has been reported by Kübler *et al.* [20].

In addition, we demonstrate a method to calculate a high-resolution B-scan individually corrected for the sub-spectral confocal functions by correcting the sub-spectral B-scans in the z -domain, transforming back to the k -domain, coherently adding the sub-spectra, and transforming the full spectrum back to the z -domain. We show this method for all three samples. For the layered TiO_2 phantom we subsequently calculate an attenuation coefficient map that displays good reproducibility of attenuation coefficients in different depths of the sample. The attenuation coefficients calculated for the *in vivo* data are comparable to values published previously [2,20,27].

Although this paper evaluates a method for extracting the focus position from B-scans acquired with a single focus setting using standard samples and preliminary *in vivo* retinal imaging, more research and studies are needed to make the presented method more robust and translate it to clinical applications. For example, the effect of astigmatism on the extracted confocal function needs further attention. The described methods require access to the complex fringe data. While complex data is in general accessible in OCT systems, enabling spectral windowing, it is worth noting that in most commercial systems, only the intensity data is available to the end user. A reliable method would greatly facilitate determination of the confocal function and subsequently attenuation coefficient calculation which has been investigated as a potential biomarker in ophthalmology [1,2], oncology [4–6,10] and cardiology [7–9]. The attenuation coefficient can potentially be used to assess the state of cells within tissue before structural changes are observed, without achieving cellular resolution. Furthermore, the confocal function with the focus position in particular plays a crucial role not only in determining the attenuation coefficient but can also serve as a foundation for other quantitative evaluations of OCT data. For instance, the focus position can have a significant impact on the accurate representation of different capillary plexuses in OCT angiography [28,29].

Funding. Heidelberg Engineering GmbH; Health~Holland, Topsector Life Sciences & Health; Holland High Tech, Topsector High Tech Systems and Materials.

Acknowledgments. We acknowledge funding by Heidelberg Engineering GmbH. The collaboration project is co-funded by the PPP Allowance made available by Health~Holland, Topsector Life Sciences & Health, and by Holland High Tech, Topsector High Tech Systems and Materials, to stimulate public-private partnerships.

Disclosures. JK: Heidelberg Engineering GmbH (F,E,P), JFdB: Heidelberg Engineering GmbH (F,P), JF: Heidelberg Engineering GmbH (E,P).

Data availability. Data underlying the results presented in this paper are not publicly available at this time but may be obtained from the authors upon reasonable request.

References

1. J. van der Schoot, K. A. Vermeer, J. F. de Boer, and H. G. Lemij, "The effect of glaucoma on the optical attenuation coefficient of the retinal nerve fiber layer in spectral domain optical coherence tomography images," *Invest. Ophthalmol. Visual Sci.* **53**(4), 2424–2430 (2012).
2. K. A. Vermeer, J. van der Schoot, H. G. Lemij, and J. F. de Boer, "RPE-normalized RNFL attenuation coefficient maps derived from volumetric OCT imaging for glaucoma assessment," *Invest. Ophthalmol. Visual Sci.* **53**(10), 6102–6108 (2012).
3. P. H. Tomlins, O. Adegun, E. Hagi-Pavli, K. Piper, D. Bader, and F. Fortune, "Scattering attenuation microscopy of oral epithelial dysplasia," *J. Biomed. Opt.* **15**(6), 066003 (2010).
4. K. Barwari, D. M. de Bruin, E. C. Cauberg, D. J. Faber, T. G. van Leeuwen, H. Wijkstra, J. de la Rosette, and M. P. Laguna, "Advanced diagnostics in renal mass using optical coherence tomography: a preliminary report," *J. Endourol.* **25**(2), 311–315 (2011).
5. K. Barwari, D. M. de Bruin, D. J. Faber, T. G. van Leeuwen, J. J. de la Rosette, and M. P. Laguna, "Differentiation between normal renal tissue and renal tumours using functional optical coherence tomography: a phase i in vivo human study," *BJU Int* **110**(8b), E415–E420 (2012).
6. Q. Q. Zhang, X. J. Wu, T. Tang, S. W. Zhu, Q. Yao, B. Z. Gao, and X. C. Yuan, "Quantitative analysis of rectal cancer by spectral domain optical coherence tomography," *Phys. Med. Biol.* **57**(16), 5235–5244 (2012).
7. F. J. van der Meer, D. J. Faber, D. M. Baraznji Sassoon, M. C. Aalders, G. Pasterkamp, and T. G. van Leeuwen, "Localized measurement of optical attenuation coefficients of atherosclerotic plaque constituents by quantitative optical coherence tomography," *IEEE Trans. Med. Imaging* **24**(10), 1369–1376 (2005).
8. C. Xu, J. M. Schmitt, S. G. Carlier, and R. Virmani, "Characterization of atherosclerosis plaques by measuring both backscattering and attenuation coefficients in optical coherence tomography," *J. Biomed. Opt.* **13**(3), 034003 (2008).

9. G. van Soest, T. Goderie, E. Regar, S. Koljenovic, G. L. van Leenders, N. Gonzalo, S. van Noorden, T. Okamura, B. E. Bouma, G. J. Tearney, J. W. Oosterhuis, P. W. Serruys, and A. F. van der Steen, "Atherosclerotic tissue characterization in vivo by optical coherence tomography attenuation imaging," *J. Biomed. Opt.* **15**(1), 011105 (2010).
10. M. Almasian, L. S. Wilk, P. R. Bloemen, T. G. van Leeuwen, M. Ter Laan, and M. C. G. Aalders, "Pilot feasibility study of in vivo intraoperative quantitative optical coherence tomography of human brain tissue during glioma resection," *J. Biophotonics* **12**(10), e201900037 (2019).
11. D. Faber, F. van der Meer, M. Aalders, and T. van Leeuwen, "Quantitative measurement of attenuation coefficients of weakly scattering media using optical coherence tomography," *Opt. Express* **12**(19), 4353–4365 (2004).
12. M. J. Girard, N. G. Strouthidis, C. R. Ethier, and J. M. Mari, "Shadow removal and contrast enhancement in optical coherence tomography images of the human optic nerve head," *Invest. Ophthalmol. Visual Sci.* **52**(10), 7738–7748 (2011).
13. K. A. Vermeer, J. Mo, J. J. Weda, H. G. Lemij, and J. F. de Boer, "Depth-resolved model-based reconstruction of attenuation coefficients in optical coherence tomography," *Biomed. Opt. Express* **5**(1), 322–337 (2014).
14. S. Yun, G. Tearney, B. Bouma, B. Park, and J. de Boer, "High-speed spectral-domain optical coherence tomography at 1.3 μm wavelength," *Opt. Express* **11**(26), 3598–3604 (2003).
15. T. G. van Leeuwen, D. J. Faber, and M. C. Aalders, "Measurement of the axial point spread function in scattering media using single-mode fiber-based optical coherence tomography," *IEEE J. Sel. Top. Quantum Electron.* **9**(2), 227–233 (2003).
16. G. T. Smith, N. Dwork, D. O'Connor, U. Sikora, K. L. Lurie, J. M. Pauly, and A. K. Ellerbee, "Automated, depth-resolved estimation of the attenuation coefficient from optical coherence tomography data," *IEEE Trans. Med. Imaging* **34**(12), 2592–2602 (2015).
17. N. Dwork, G. T. Smith, J. M. Pauly, and A. K. E. Bowden, "Automated estimation of oct confocal function parameters from two b-scans," in *Conference on Lasers and Electro-Optics*, (Optica Publishing Group, 2016), p. AW10.4.
18. N. Dwork, G. T. Smith, T. Leng, J. M. Pauly, and A. K. Bowden, "Automatically determining the confocal parameters from oct b-scans for quantification of the attenuation coefficients," *IEEE Trans Med Imaging* **38**(1), 261–268 (2019).
19. S. Stefan, K. S. Jeong, C. Polucha, N. Tapinos, S. A. Toms, and J. Lee, "Determination of confocal profile and curved focal plane for oct mapping of the attenuation coefficient," *Biomed. Opt. Express* **9**(10), 5084–5099 (2018).
20. J. Kübler, V. S. Zoutenbier, A. Amelink, J. Fischer, and J. F. de Boer, "Investigation of methods to extract confocal function parameters for the depth resolved determination of attenuation coefficients using OCT in intralipid samples, titanium oxide phantoms, and in vivo human retinas," *Biomed. Opt. Express* **12**(11), 6814–6830 (2021).
21. R. Leitgeb, M. Wojtkowski, A. Kowalczyk, C. K. Hitzenberger, M. Sticker, and A. F. Fercher, "Spectral measurement of absorption by spectroscopic frequency-domain optical coherence tomography," *Opt. Lett.* **25**(11), 820–822 (2000).
22. A. L. Oldenburg, C. Xu, and S. A. Boppart, "Spectroscopic optical coherence tomography and microscopy," *IEEE J. Sel. Top. Quantum Electron.* **13**(6), 1629–1640 (2007).
23. R. Michels, F. Foschum, and A. Kienle, "Optical properties of fat emulsions," *Opt. Express* **16**(8), 5907–5925 (2008).
24. D. M. de Bruin, R. H. Bremmer, V. M. Kodach, R. de Kinkelder, J. van Marle, T. G. van Leeuwen, and D. J. Faber, "Optical phantoms of varying geometry based on thin building blocks with controlled optical properties," *J. Biomed. Opt.* **15**(2), 025001 (2010).
25. R. Navarro, J. Santamaria, and J. Bescos, "Accommodation-dependent model of the human eye with aspherics," *J. Opt. Soc. Am. A* **2**(8), 1273–1281 (1985).
26. J. F. de Boer, B. Cense, B. H. Park, M. C. Pierce, G. J. Tearney, and B. E. Bouma, "Improved signal-to-noise ratio in spectral-domain compared with time-domain optical coherence tomography," *Opt. Lett.* **28**(21), 2067–2069 (2003).
27. H. Hammer, D. Schweitzer, E. Thamm, A. Kolb, and J. Strobel, "Scattering properties of the retina and the choroids determined from oct-a-scans," *Int. Ophthalmol.* **23**(4/6), 291–295 (2001).
28. E. A. T. Say, S. Ferenczy, G. N. Magrath, W. A. Samara, C. T. L. Khoo, and C. L. Shields, "Image quality and artifacts on optical coherence tomography angiography: Comparison of pathologic and paired fellow eyes in 65 patients with unilateral choroidal melanoma treated with plaque radiotherapy," *Retina* **37**(9), 1660–1673 (2017).
29. A. Tomlinson, B. Hasan, and B. J. Lujan, "Importance of focus in oct angiography," *Ophthalmol. Retina* **2**(7), 748–749 (2018).